Journal of Alloys and Compounds 962 (2023) 171166

Contents lists available at ScienceDirect

Journal of Alloys and Compounds

journal homepage: www.elsevier.com/locate/jalcom

Heat treatment response and mechanical properties of a Zr-modified AA2618 aluminum alloy fabricated by laser powder bed fusion

Marvin Schuster[a,b], Anthony De Luca[a], Dagmara Kucajda[a], Ehsan Hosseini[a], Remo Widmer[a], Xavier Maeder[a], Christian Leinenbach[a,b,*]

[a] Empa - Swiss Federal Laboratories for Materials Science and Technology, Überlandstrasse 129, 8600 Dübendorf, Switzerland
[b] École Polytechnique Fédérale de Lausanne (EPFL), Laboratory for Photonic Materials and Characterization, 1015 Lausanne, Switzerland

ARTICLE INFO

Keywords:
Laser powder bed fusion
Selective Laser Melting
2618
Microstructure
Heat treatment
Mechanical properties

ABSTRACT

Additive manufacturing of commercial materials designed for casting is challenging, particularly for hot-crack-susceptible alloys. Adding Zr to Al alloys has a positive effect on part consolidation by suppressing hot cracks and enabling nanoprecipitation hardening. Despite the special solidification conditions during laser powder bed fusion and the use of modified alloy chemistries, the heat treatments that were optimized decades ago for cast or wrought alloys are still applied. These treatments thus do not optimally exploit the full potential of novel alloys tailored for additive manufacturing. This work investigates the microstructure, precipitate formation, and mechanical properties of a Zr-modified 2618 Al alloy via laser powder bed fusion. A three-step heat treatment yields several nanometric phases, including L1$_2$-Al$_3$Zr, S-Al$_2$CuMg, and Mg$_2$Si, which strengthen the alloy. Tensile tests reveal ultimate and yield strengths of 478 ± 7 MPa and 401 ± 3 MPa, respectively, and an elongation to fracture of 9.2 ± 1.1%. These values match conventionally manufactured and heat-treated 2618 standards and exceed T6 properties. The results emphasize the need to adapt heat treatments for additive manufacturing, not just materials.

1. Introduction

Additive manufacturing (AM), also known as 3D printing, belongs to the family of generative manufacturing processes and allows the rapid production of near-net-shape parts. The most widely used AM process for metal is laser powder bed fusion (LPBF). Within the process, a thin layer of powder is deposited on a build platform and selectively melted with a focused laser beam. After solidification, another powder layer is applied and metallurgically bonded to the previously consolidated layer. The repetition of this cycle allows the tool-free production of complex geometries in comparatively little time with a minimal quantity of waste [1].

Among the various materials that can be manufactured, high-strength aluminum alloys are of high interest, for example often used in aerospace or the automotive industry, because of their excellent strength-to-weight ratio. Together with the possibilities of AM to produce topology-optimized structures with intricate geometries and increased functionalities, along with a reduction in the number of parts as compared to a conventionally manufactured component, a wide range of applications is opening up, lowering for example the buy-to-fly ratio in aerospace or allowing more eco-friendly applications in automotive [2]. However, the processing of high-strength aluminum alloys presents inherent difficulties. Process-related difficulties are primarily caused by the high melt pool temperatures and extreme heating and cooling rates [3,4]. Material-related difficulties include the low absorptivity of Al in the range of wavelengths of commonly used laser types (Nd:YAG and fiber lasers), the melt pool instability due to the high thermal conductivity, the low viscosity of Al melts, and the low wettability due to the oxide layer on consolidated layers and powder particles [5,6].

These process- and material-related characteristics can lead to the formation of defects in the component, particularly if the process parameters are not precisely ascertained or if alloys not tailored to the unique processing conditions are used. If the energy density is too high, volatile alloying elements, such as Mg, Zn, or Li, evaporate and form bubbles in the melt pool. These gas pores, which are spherically shaped due to the minimization of surface energy, are entrapped in the microstructure during the rapid progression of the solidification front. If the

---

* Corresponding author at: Empa - Swiss Federal Laboratories for Materials Science and Technology, Überlandstrasse 129, 8600 Dübendorf, Switzerland.
E-mail address: christian.leinenbach@empa.ch (C. Leinenbach).

https://doi.org/10.1016/j.jallcom.2023.171166
Received 25 March 2023; Received in revised form 1 June 2023; Accepted 26 June 2023
Available online 27 June 2023
0925-8388/© 2023 The Authors. Published by Elsevier B.V. This is an open access article under the CC BY license (http://creativecommons.org/licenses/by/4.0/).

energy density is too low, disk-shaped "lack-of-fusion" pores can form due to insufficient overlap of adjacent melt pools, and they often contain non-molten powder [7,8]. Another frequently occurring defect is cracking, particularly in non-weldable high-strength aluminum alloys [9,10]. The formation of cracks, which can extend over several layers, is caused by the pronounced elemental segregation in alloys with a high solidification interval. The hot cracking susceptibility can be significantly reduced by adjustments of the alloy composition [8,11].

Hitherto, the vast majority of work on AM has focused on optimizing the processing conditions for printing conventional alloys. This overlooks the fact that these alloys were originally designed and optimized for processing routes other than AM, such as casting or forging. Although these cast-grade eutectic or near-eutectic Al alloys, which often contain Si (AlSi10Mg, AlSi12) or Ce (Al10Ce), can be additively manufactured crack-free and with high density, their mechanical properties are usually unsatisfactory for broader application [7,12].

When developing novel alloys adapted to additive manufacturing together with suitable heat treatment processes, it is essential to consider the unique, distinctive process conditions in LPBF. The process is characterized by melt pool temperatures of over 2000 °C, far-from-equilibrium solidification conditions with cooling rates exceeding 10^7 K/s as well as intrinsic heat treatment due to the layer-wise build-up. This can result in the formation of metastable phases and supersaturation of the matrix [5,13–15]. Those pose particular challenges, which often prevent the use of conventional materials and established heat treatment procedures.

In recent years, intensive research has been carried out on novel or modified conventional high-strength Al alloys adapted to the unique process conditions of AM. Particularly noteworthy is the development of alloys containing rare earth and transition metals, in particular Sc and/or Zr [16,17]. Driven by their limited solubility in Al, these elements cause the formation of primary $L1_2$-Al_3Sc (stable) and $L1_2$-Al_3Zr (metastable) precipitates, which form upon cooling in the melt. Due to the very low lattice mismatch (+0.75% for Al_3Zr and +1.32% for Al_3Sc [18]) of their $L1_2$ structure compared to the Al matrix, they provide ideal heterogeneous nucleation sites for the Al crystals, hence being very effective in inducing a fine-grained, equiaxed microstructure. Consequently, this simple modification allows the fabrication of crack-free components with excellent strength, ductility, and toughness. Besides, the use of Sc and/or Zr enables precipitation strengthening via post-process heat treatment. Both Zr and Sc are supersaturated in solid solution due to solute trapping caused by LPBF's characteristic rapid solidification. The very low diffusivity of Zr and Sc in Al (1.20×10^{-20} m^2s^{-1} and 1.98×10^{-17} m^2s^{-1} at 400 °C, respectively [19]), leads to the formation of nanometer-sized secondary $L1_2$-Al_3M precipitates that considerably increase the strength and are stable at high temperatures.

The mechanism of primary $L1_2$-Al_3M induced grain refinement to reduce susceptibility to hot cracking as well as secondary $L1_2$-Al_3M precipitation hardening, which have already been extensively investigated for 5xxx alloys [16,17,20,21], could be successfully applied to other alloy classes that also exhibit a pronounced solidification interval. Although much less extensively researched than the Al-Si(-Mg) and Al-Mg-Sc(-Zr) alloy systems, the 2xxx series, with Al and Cu as the main alloying elements, is particularly noteworthy. This non-weldable, heat-treatable alloy class shows pronounced hot cracking issues during production by LPBF [22,23]. Although some unmodified alloys (2022, 2024, 2618) were successfully produced crack-free within a very narrow process window, significant porosity or geometry restrictions (e.g. single tracks, wall structures, small geometries) always had to be accepted [24,25].

Zhang et al. were able to achieve defect-free consolidation of Al-4.2Cu-2.0Mg-0.6Mn (wt%) using LPBF by adding 2 wt% pure Zr particles to the feedstock powder [26,27]. However, the mechanical properties in the as-built condition of this very simple, 'in-situ produced' alloy, showing a yield strength (YS) and ultimate tensile strength (UTS) of 446 MPa and 451 MPa, respectively, were not improved by a post-process heat treatment. Noteworthy, the latter is a key feature to increase the strength of Al-Cu alloys. Due to the relatively high diffusivity of Cu and Mg (4.0×10^{-14} m^2s^{-1} and 9.9×10^{-14} m^2s^{-1} at 500 °C, respectively [28]) in Al, solution annealing followed by an aging step is typically applied to induce precipitation of the most important strengthening phase S-Al_2CuMg. Wang et al. were able to produce a dense but cracked, very fine-grained microstructure with mechanical properties of 376 MPa for YS and 441 MPa for UTS at an elongation to fracture of 14% by adding 1.3 wt% Zr to a 2024 alloy [29]. After a T6 heat treatment, an increase to 402 MPa and 486 MPa was obtained for YS and UTS, respectively. Li et al. investigated different compositions of an Al-Cu-Mg-Mn-Zr alloy based on a 2024 by thermodynamic simulations [30]. The Zr modification resulted in a duplex microstructure of fine equiaxed grains and coarse columnar grains, each of which demonstrated superior mechanical properties with increasing Zr content. The variant with the best mechanical properties contained 3.72 wt % Zr and achieved a YS of 561 MPa, UTS of 580 MPa, and elongation to fracture of 6%.

In a recent work, the present authors were able to produce a crack-free microstructure with an average microhardness of 1360 ± 74 MPa in the as-built condition by Zr modification of a 2618, while observing a much more complex precipitation behavior than for cast 2618 [31]. In general, apart from the above-mentioned studies, only few other studies exist which characterize the mechanical properties, in particular with regard to precipitation, which is of central relevance for 2xxx series alloys [7,13,32,33]. However, a comprehensive understanding of the precipitate formation and its correlation with the mechanical properties is vital, particularly concerning the ongoing development and future application of 2xxx series Al-Cu alloys tailored to LPBF.

Traditional heat treatments (for example T6, T61, T62, T861) primarily target the precipitation of S-Al_2CuMg, which is responsible for the strength increase in many 2xxx series alloys. These heat treatments, which have been optimized for conventional alloys, might not be well suited for the formation of a population of finely dispersed, nanometer-sized $L1_2$-Al_3Zr, which are fundamental for the strength increase of Zr-containing alloys. In conventionally produced 2618, the manufacturing process is typically followed by a heat treatment consisting of solution annealing, quenching, and artificial aging. Solution annealing below the solidus temperature at about 530 °C and subsequent quenching to room temperature (RT) is intended to dissolve the precipitates formed in the as-processed state and to trap the elements needed for a successive aging step into solid solution [34]. In 2618, Al_2CuMg, Al_2Cu, Al_7Cu_4Ni, $Al_7Cu_2(Fe,Ni)$, as well as Al_9FeNi are commonly found, whereby the latter two do not dissolve during heat treatment, but fragment and spheroidize [35]. The artificial aging at 180–200 °C exploits the increasing diffusion of the precipitate-forming elements (mainly Cu, Mg) with increasing temperature [28]. It aims at the formation of homogeneously distributed nanometer-sized precipitates, primarily of the major strengthening phase S-Al_2CuMg but also Mg_2Si, Al_2Cu, and Al_9FeNi [36,37]. While these two-step heat treatments are commonly used for conventional 2xxx series alloys, Croteau et al. were able to identify an aging step at 400 °C for Zr-modified 5xxx alloys as optimal for precipitation of secondary, strength-enhancing $L1_2$-Al_3Zr [16].

This work is a continuation of our previous work [31] and investigates the microstructure of a Zr-modified 2618 optimized for LPBF process conditions, with particular emphasis on the microstructure and precipitate formation as well as the associated mechanical properties after various heat treatments. High strength is not only achieved by precipitation of secondary nanometer-sized Al_3Zr but also by precipitation of homogeneously dispersed, nanometer-sized Al_2CuMg by combining the approach for Zr-modified 5xxx series alloys (Addalloy™, Scalmalloy®) of these alloys with a T6 in three-step heat treatment.

Table 1
Chemical composition. Nominal composition of commercial and Zr-modified 2618 as well as ICP-OES measurement of the chemical composition for the as-received powder and after LPBF consolidation (in wt%).

	Al	Cu	Mg	Zr	Fe	Ni	Si	Ti	Zn	Sn
2618, nominal	Bal.	1.80–2.70	1.20–1.80	-	0.90–1.40	0.80–1.40	0.15–0.25	0.00–0.20	0.00–0.15	-
This work, nominal	Bal.	1.90–2.70	2.00–2.20	1.80–2.00	0.90–1.30	0.90–1.20	0.10–0.25	0.04–0.10	$\leq$ 0.10	-
Powder, ICP-OES	Bal.	2.36 ± 0.10	1.95 ± 0.02	1.71 ± 0.05	1.17 ± 0.01	0.97 ± 0.01	0.24 ± 0.01	< 0.01	0.01 ± 0.001	0.05 ± 0.001
As-built, ICP-OES	Bal.	2.40 ± 0.09	1.55 ± 0.03	1.71 ± 0.05	1.18 ± 0.03	0.97 ± 0.02	0.23 ± 0.01	< 0.01	< 0.01	< 0.03

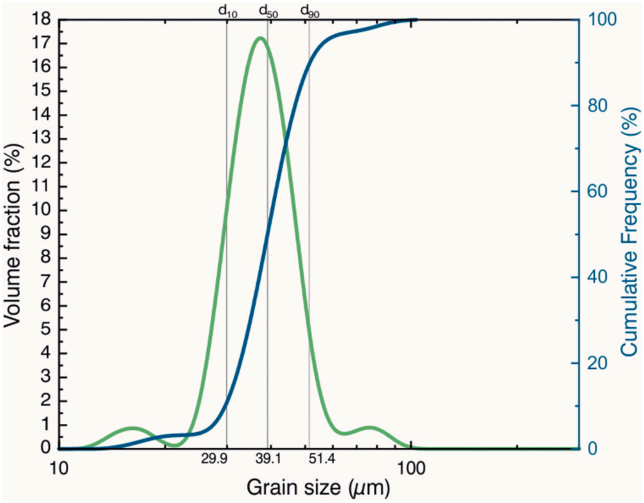

Fig. 1. Powder size distribution. Evaluated by laser diffraction measurements. The powder shows a right-skewed, Gaussian-shaped size distribution with a noticeable fraction of fine, sub 20 μm and coarse, super 70 μm grains. A d_{50} of 39.1 μm, with a d_{10} of 29.9 μm and a d_{90} of 51.4 μm is estimated.

2. Materials and methods

2.1. Powder feedstock

The Zr-modified 2618 powder was produced by ECKA Granules Germany GmbH with the nominal chemical composition given in Table 1. Compared to standard 2618, the Mg content was slightly increased and Zr was added to adapt the alloy to LPBF based on a previous study of an Al-Cu-Mg-Zr model alloy [32]. The feedstock powder composition was analyzed by inductively coupled optical emission spectroscopy (ICP-OES). For that, the powder was dissolved with sodium hydroxide solution (40%) and neutralized with hydrochloric acid (37%). The sample was completely dissolved using a medium pressure microwave oven at 180 °C for 30 min and then analyzed using the Agilent 5110. The particle size distribution was determined by laser diffraction (Fig. 1) and had a d_{50} of 39.1 μm (d_{10}-d_{90} = 29.9–51.4 μm), showing a slightly right-skewed, leptocurtic distribution with a noteworthy fraction of both fine (<20 μm) and coarse (>70 μm) particles. The bulk density of the powder according to EN ISO 3923/1 and the flow rate at a funnel size of 2.54 mm according to EN ISO 4490 is 1.38 g/cm^3 and 65.5 s/50 g, respectively. The powder shows a predominantly spherical morphology with many satellite particles and splatters (Fig. 2). While no large entrapped porosity is observed in the powder cross-section, nanopores on GBs are occasionally present. Numerous primary Al_3Zr precipitates are evident within the predominantly equiaxed grains. A eutectic phase on the GBs is also evidenced.

2.2. Laser powder bed fusion

The LPBF experiments were performed on a Sisma MySint 100, which is equipped with a 1070 nm Yb fiber laser, enabling a maximum laser power of 200 W at a spot size of 55 μm. During consolidation, Ar 4.6 shielding gas (99.996%) was used at atmospheric pressure to keep the oxygen concentration in the build chamber below 100 ppm O_2. The components were fabricated on a build platform of AlSi10Mg with a diameter of 100 mm and subsequently cut by electro-discharge machining (EDM). Since 2xxx series alloys are known for their natural aging behavior when exposed to RT, the samples were stored in a freezer at – 26 °C between each preparation and characterization step. The optimum LPBF process parameters were determined in a previous study [31]. The following parameter set was employed for all conducted experiments: Laser power 168 W, scan speed 149 mm/s, and hatch distance 0.117 mm. The layer thickness was fixed at 0.03 mm. A bidirectional scanning strategy with 90° rotation between layers was chosen.

2.3. Microstructure characterization

The densities of the consolidated parts were measured using Archimedes' principle in ethanol. The theoretical density of the alloy at RT was estimated at 2.80 g/cm^3 by using Thermo-Calc® 2021 with the TCAL6 database, which is used to calculate the relative density of the manufactured samples reported herein. Subsequently, the specimens were cut parallel to the build direction using a precision cutting machine and cold mounted in epoxy resin. This was followed by grinding with #2500 grit abrasive paper and polishing with 6 μm and 1 μm diamond suspension. The final polishing step was performed using a 50 nm colloidal silica solution.

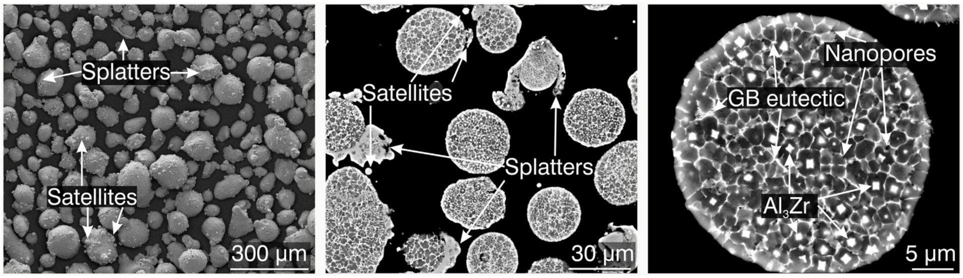

Fig. 2. Powder analysis. SEM-EDS/BSD image of the fresh powder's surface and cross-section. The powder shows decent sphericity with many satellite particles and a high number of splatters located around the particles. Numerous primary Al_3Zr precipitates can be seen within grains. The GBs are covered by a continuous eutectic layer formed by segregation. Nanopores are rarely detected on the GBs. Figure taken from [31].

The microstructure was analyzed using scanning electron microscopy (SEM) on both an FEI NanoSEM 230 and an FEI Quanta 650 FEG, equipped with a backscatter electron detector (BSD) for Z-contrast imaging. The chemical analysis was performed using energy-dispersive X-ray spectroscopy (EDX) detectors from Oxford Instruments and Thermo Fisher. The electron acceleration voltage for all SEM investigations was 12 kV. The texture analysis was conducted on a Tescan Mira using electron backscatter diffraction (EBSD). The polished sample was tilted at a surface angle of 70° and the SEM conditions for EBSD mapping were 20 kV acceleration voltage at 10 nA. A step size of 200 nm was used to scan the 200 × 200 µm-sized region of interest. The phase analysis was performed by X-ray diffraction (XRD) on a Bruker D8 diffractometer with Cu-Kα radiation, equipped with a 0.012 mm thick Ni filter. Rietveld refinements were performed using TOPAS-Academic v6 based on an experimentally determined TCHZ peak shape from LaB_6 reference measurements [38]. Refined parameters include the unit cell dimensions, the scale factors, and the crystallite size based on a Lorentzian contribution to peak broadening. Preferred orientation corrections were applied only for the Al_9FeNi phase by means of spherical harmonics.

For scanning transmission electron microscopy (STEM), lamellae were extracted perpendicular to the build direction using an FEI Helios NanoLab 600i focused ion beam (FIB) and placed on a Mo grid. STEM was performed on an FEI Titan Themis microscope, equipped with a probe spherical aberration corrector. The acceleration voltage for the electron beam was 300 kV and a 25 mrad probe convergence semiangle was used. STEM imaging was done using a high angle annular dark-field (HAADF) detector with a 53 mrad inner/200 mrad outer collection semiangle. Chemical analysis was performed with the SuperEDX system (ChemiSTEM technology) with four silicon drift detectors for energy-dispersive X-ray spectroscopy (EDX). The phase analysis used the Al-K, Mg-K, Cu-L, Fe-L, Ni-L, Si-K, Sn-L, O-K, and Zr-K lines and was conducted using Velox 3.0. Due to a high background level in the O signal, the reported quantification for all other elements was done without considering O. The reported O map was done by counting all elements. To improve the counting statistic per pixel, a pre-filtering was applied. All TEM imaging was done with the build direction being out of the plane.

2.4. Heat treatment

To identify the solidus and liquidus temperature of the alloy as well as the solvus temperature of intermetallic phases, differential scanning calorimetry (DSC) was conducted using a Netzsch DSC 404 C Pegasus thermal analyzer. A sample with a mass of 14.5 mg was ground on all sides with SiC grinding paper to #4000 grid to ensure a high contact area between the crucible and the sample. The reaction chamber was inertized using argon 6.0 (99.9999% Ar) with a continuous gas flow of 40 ml/min. The Al_2O_3 crucibles were heated at a rate of 10 K/min, from RT to 800 °C.

The heat treatment study was carried out on a Nabertherm LH 15/14 and a Nabertherm LH 30/14, which temperatures were calibrated before the experiment. All heat treatments were conducted in air and terminated by water quenching. After solutionizing and quenching, the samples were heat-treated immediately at the final step to avoid natural aging, or placed into a freezer until further sample preparation and measurement was performed.

2.5. Mechanical testing

Microhardness measurements were conducted on a Fischerscope HM2000 hardness tester. A load of 2000 mN, for an indentation time of 5 s, was employed. The reported microhardness values correspond to the average of at least ten measurement points per sample.

Tensile tests of the cylindrical dog-bone samples, which were subjected to the various stages of heat treatment, were performed on a walter+bai LFMZ-50-HM central spindle testing machine. For each selected aging condition, three specimens fabricated parallel and perpendicular to the build direction were tested. The final geometry according to ASTM E9–19 was produced by precision turning and had a total length of 58 mm, gauge length of 20 mm, and gauge diameter of 4 mm. An Epsilon side entry extensometer with a datum gauge length of 10 mm and a travel range of 10% was used to directly measure the strain in the middle section of the gauge length. However, since a number of specimens ruptured outside the extensometer datum gauge, the machine displacement records were used to determine the strain evolution until rupture. Details on the calibration of the machine displacement signal based on the extensometer readings and the strain calculation are given in the Supplementary material. Note that the as-built tensile test specimens were stored at RT for one month between fabrication and machining because of a shortage in personnel in the workshop during the Covid-19 pandemic.

Table 2

Heat treatments performed. Temperatures and times for the two heat treatments used, a two-step T6 and a 3-step heat treatment including a high temperature aging step.

Heat treatment	Step 1	Step 2	Step 3
T6	530 °C, 1–6 h	180 °C, 1–6 h	-
3 S	400 °C, 1–48 h	530 °C, 1–6 h	180 °C, 1–10 h

3. Heat treatment design

The first isothermal aging step at 400 °C, which is only applied in the three-step heat treatment (Table 2), takes advantage of the process-inherent rapid solidification in LPBF, which leads to a high proportion of Zr in solution by solute trapping. This Zr incorporated in the matrix is consequently available for the precipitation of secondary, nanometric $L1_2$-Al_3Zr. Croteau et al. identified a temperature of 400 °C as ideal to form these $L1_2$-Al_3Zr precipitates in the Zr-modified 5xxx series alloy Addalloy™ [16]. Since the objective of this step is the formation of these precipitates with optimal size, spacing, and volume fraction, and the same temperature was found to be reasonable in previous studies on Zr-modified 2xxx series alloys, it consequently is also used in this study [32]. The phase fraction calculation shown in Fig. 3 confirms not only the stability of the Al_3Zr phase at 400 °C but also shows the dissolution of Al_2CuMg on GBs and the formation of Al_7Cu_2Fe within grains for this step.

The following solution annealing and quenching in the second step of the three-step heat treatment, representing the first step of the T6 heat treatment (Table 2), aim at dissolving Al_7Cu_2Fe and Mg_2Si to allow for an additional aging step. Ostwald ripening should lead to coarsening of Al_9FeNi and its fraction is expected to slightly increase during solutionizing. Based on literature data on 2618 in conjunction the measured solidus (568 °C) and liquidus (644 °C) temperature using DSC (Fig. S1), a solutionizing temperature of 530 °C was selected, which avoids incipient melting of grain boundary (GB) phases [36,37].

If solution annealing is applied directly after production without a high temperature aging step of 400 °C, the duration of this annealing step, used to promote the formation of $L1_2$-Al_3Zr with optimal size, volume fraction, and number density, could be prolonged. While the coherent, metastable $L1_2$-Al_3Zr are known to exhibit very good high-temperature stability due to their low lattice mismatch (0.52%) as well as low diffusion coefficient ($1.20{\cdot}10^{-20}$ m^2s^{-1} at 400 °C), the solution annealing time has to be kept as short as possible to minimize the risk of overaging or potentially transforming the $L1_2$-form into the stable, incoherent $D0_{23}$-form as well as to avoid excessive grain growth. Both would have a negative effect on the mechanical properties. Studies on (Sc,Zr)-modified conventional Al-Cu alloys have already demonstrated a positive effect of a three-step heat treatment [39]. Therefore, this work compares the microstructure and mechanical properties of a three-step heat treatment with those of a T6 heat treatment for

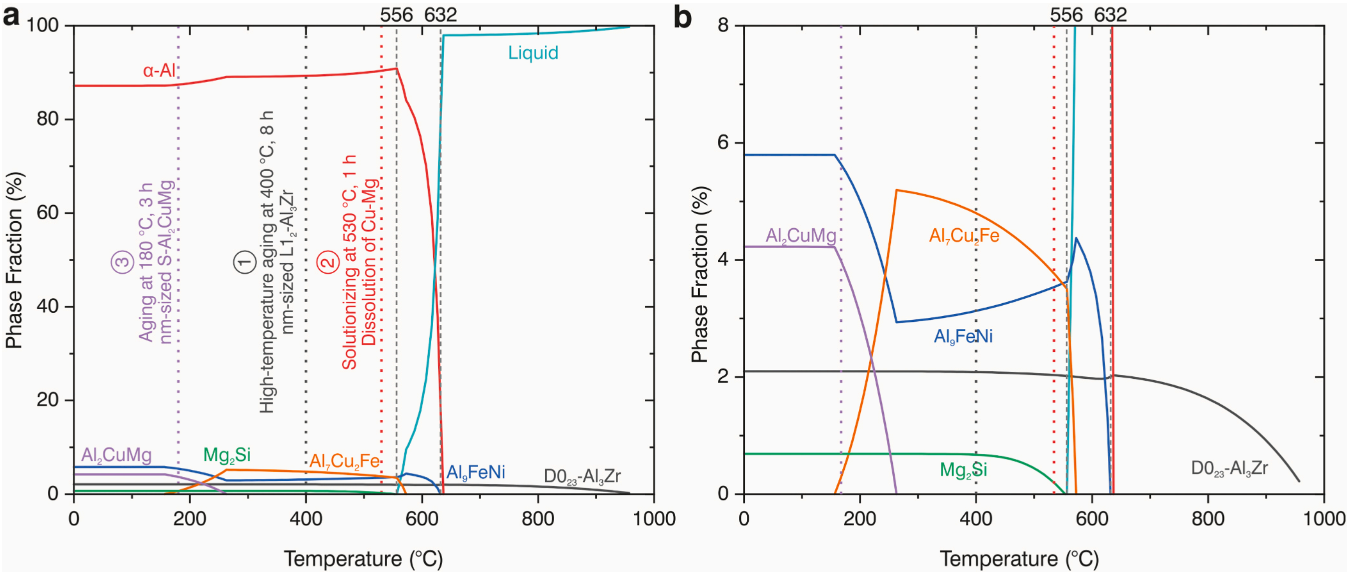

Fig. 3. Phase formation in the Zr-modified 2618 and heat treatment temperature selection. a) Phase fraction simulations predict the formation of Al_7Cu_2Fe and dissolution of primary Al_2CuMg during the first high-temperature aging step at 400 °C. Mg_2Si and a partial fraction of Al_7Cu_2Fe are dissolved during a second solutionizing step at 530 °C. At a third aging step at 180 °C, nanometric, rod-shaped Al_2CuMg re-precipitates within the grains. It should be noted that the term "solutionizing" in this work refers to the highest degree of dissolution of Cu-Mg rich compounds, as Al_3Zr remain stable even above the liquidus temperature of the Al matrix. b) Zoom in on the relevant area for better readability.

Zr-modified AA2618 produced by LPBF.

After quenching from the solutionizing temperature, isothermal aging at 180 °C followed as the third and final step, aiming at the formation of nanometric, rod-shaped S-Al_2CuMg within grains. Thermo-Calc® calculations prove the stability of this phase at 180 °C. The three-step heat treatment performed, which primarily aims at the formation of the nanometric and strength-enhancing precipitates $L1_2$-Al_3Zr as well as S-Al_2CuMg, is shown in Fig. 3. The two heat treatments applied are listed in Table 2.

4. Results

4.1. Microstructure in as-fabricated samples

As shown in our previous work, the optimized process parameters allow for a part density of 99.93 ± 0.02% for specimens fabricated with fresh powder [31]. Metallographic cross-sections parallel to the build direction display a small area fraction of circular pores, about 10–25 µm in size. Melting and subsequent consolidation reduce the Mg content from 1.95 ± 0.02 wt% in the feedstock powder to 1.55 ± 0.03 wt% in the as-fabricated component [31].

A detailed description of the as-built microstructure and precipitation has been performed and reported in our previous study [31], with the most important features transcribed herein. Melt pools are 150–200 µm wide and 100–150 µm deep and have an overall semi-circular shape. The very distinct, trimodal microstructure within the melt pools reflects three different solidification morphologies which are formed sequentially in time. At the edge of the melt pool, a 5–20 µm thick band of ~0.5 µm fine and equiaxed grains solidifies first, frequently containing cuboidal $L1_2$-Al_3Zr precipitates with an edge length of about 50–100 nm. In the further course of the melt pool solidification, a band of 5–15 µm long and 1–3 µm wide columnar-dendritic grains is formed, inside which no Al_3Zr precipitates are visible. The remaining, and largest, part of the melt pool, which solidifies last, consists of 1–3 µm sized, equiaxed grains. The average grain size measured by EBSD is 1.46 µm. Most GBs are covered by a coherent Fe-Ni-Cu rich film, which consists predominantly of Al_9FeNi, but also of Al_2CuMg, AlCu, and Mg_2Si. Very sporadically, 0.5–1.5 µm long, 0.1–0.2 µm wide $D0_{23}$-Al_3Zr are visible. The microhardness in the as-built state averages 1360 ± 74 MPa with an indentation modulus of 94 ± 3 GPa.

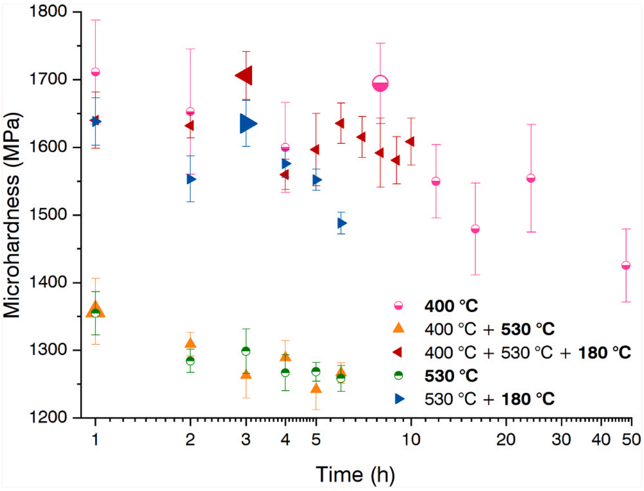

Fig. 4. Microhardness measurements. Microhardness was measured after various heat treatment durations. The time of the respective temperature printed in bold fonts was varied, whereby the peak hardness (enlarged symbol) was used for subsequent steps in each case, hence 400 °C, 8 h; 530 °C, 1 h; 180 °C, 3 h.

While the microstructure characterization was performed on specimens fabricated with fresh powder, the tensile test specimens, in particular, were fabricated with re-used powder that was stored for approximately 12 months. During this time, the powder was stored in the laboratory in a sealed powder container containing a silica gel bag to absorb potential moisture. A subsequently performed, second parameter optimization indicated that the process parameters for the highest density are unchanged, but the achievable maximum density is lower. Thus, the use of recycled powder from the previous print jobs led to a reduction in density to 99.73 ± 0.01% for the tensile test specimen. Aluminum powder degradation is a known issue [40,41]. Occasional

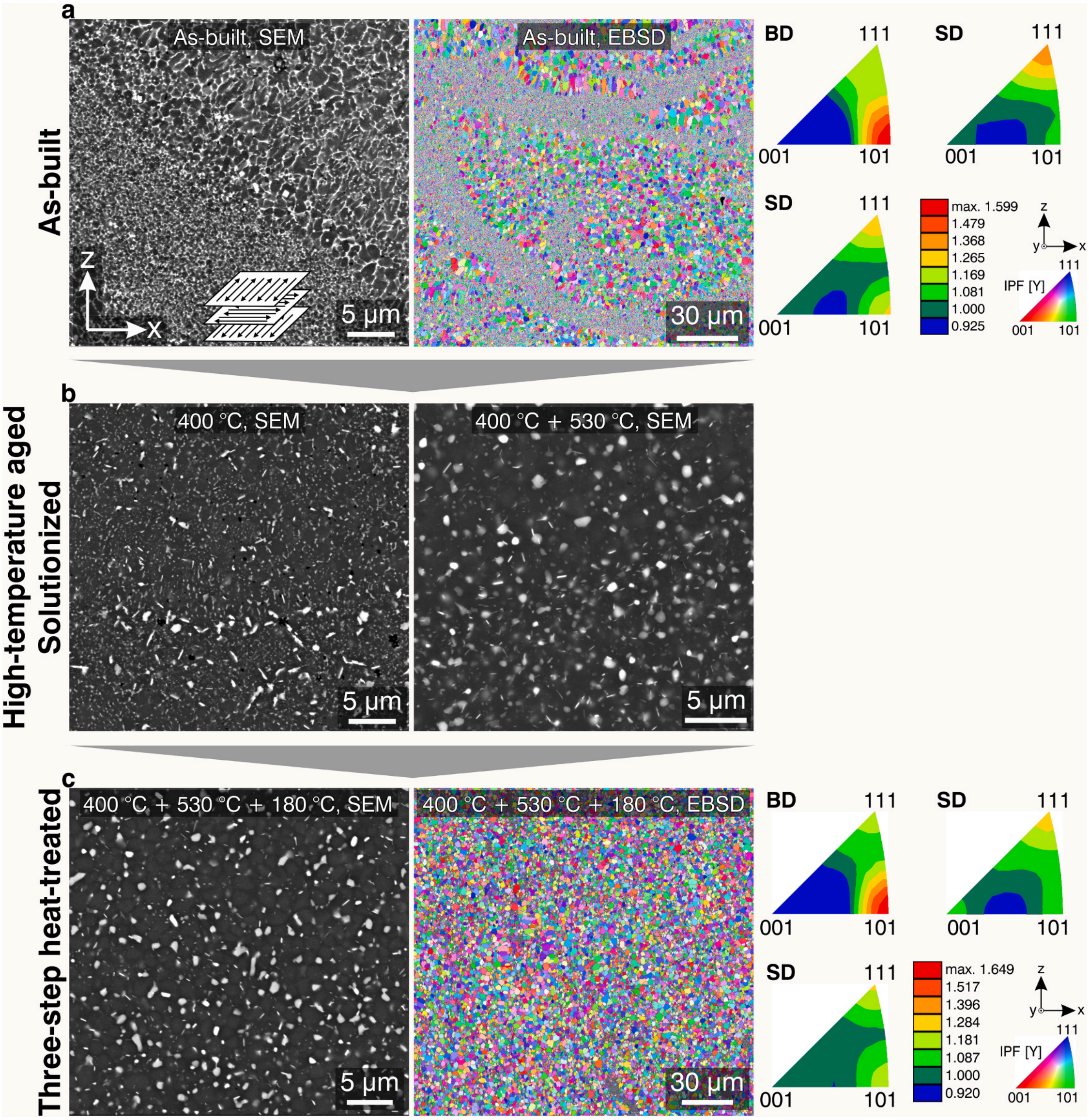

Fig. 5. Microstructure evolution induced by different heat treatment steps. SEM-BSD micrographs, as well as EBSD maps, show representative microstructures after various heat treatments. a) As-built and schematic build-up strategy. b) 400 °C, 8 h, and 400 °C + 530 °C, 1 h. c) 400 °C, 8 h + 530 °C, 1 h + 180 °C, 3 h. After 400 °C, the melt pool boundaries are populated by both fine and coarse rod-shaped Al_3Zr precipitates. The melt pool contours are not discernible anymore. After solutionizing, the formerly continuous GB phase is segmented. After the final aging, two main types of block-shaped precipitates are recognizable. Texture is low, with significant grain growth observable during heat treatment.

spherical pores, 10–50 µm in diameter, as well as 50–150 µm long, 10–30 µm wide lack-of-fusion defects, were evident, which both could not be observed when using fresh powder. Apart from the higher pore density, no differences in the chemical composition, grain size, and phases present could be observed.

4.2. Precipitation and microhardness evolution during heat treatment

To identify the optimal heat treatment for the modified alloy, the duration of each step of the heat treatment was varied. The most suitable duration is then determined based on microhardness measurements. The cross-sections of selected samples are examined with regard to microstructure and precipitation characteristics. Detailed hardness curves for the respective heat treatment steps can be found in Fig. 4. Noteworthy, the microstructure characterization is limited to the three-step heat treatment, while the T6 heat treatment is used as a comparison for microhardness and tensile test properties.

After 1 h at 400 °C, the microhardness increases by 351 MPa, from 1360 ± 74 MPa in the as-fabricated state to 1711 ± 76 MPa (Fig. 4). Upon further aging, the microhardness decreases to a value of 1425 ± 54 MPa after 48 h. However, a second microhardness maximum of 1695 ± 59 MPa is obtained after 8 h, an increase of 25% compared to the as-built condition and comparable to the microhardness after 1 h. While the 1 h treatment displays a similar hardness value as the 8 h treatment, this state might be unstable, i.e. it might result from the precipitation of Cu-Mg rich phases instead of the preferred nm-sized $L1_2$-Al_3Zr. In this view, a heat treatment duration of 8 h is preferred and applied for the further experiments as the microstructure is more stable and not transient. Noticeable microstructural changes can be observed by SEM-BSD (Fig. 5b). The analysis of the precipitates after the 400 °C heat treatment is based on point EDX measurements as well as ThermoCalc® calculations (Fig. S5, Table S1) and thus only allows for a rough estimation of the main elements contained at these locations. Agglomerations of blocky, 500–800 nm-sized Fe-Ni-rich phases have formed. The melt pool contours are no longer visible. In particular along the former melt pool contours and within the fine-grained region, a high

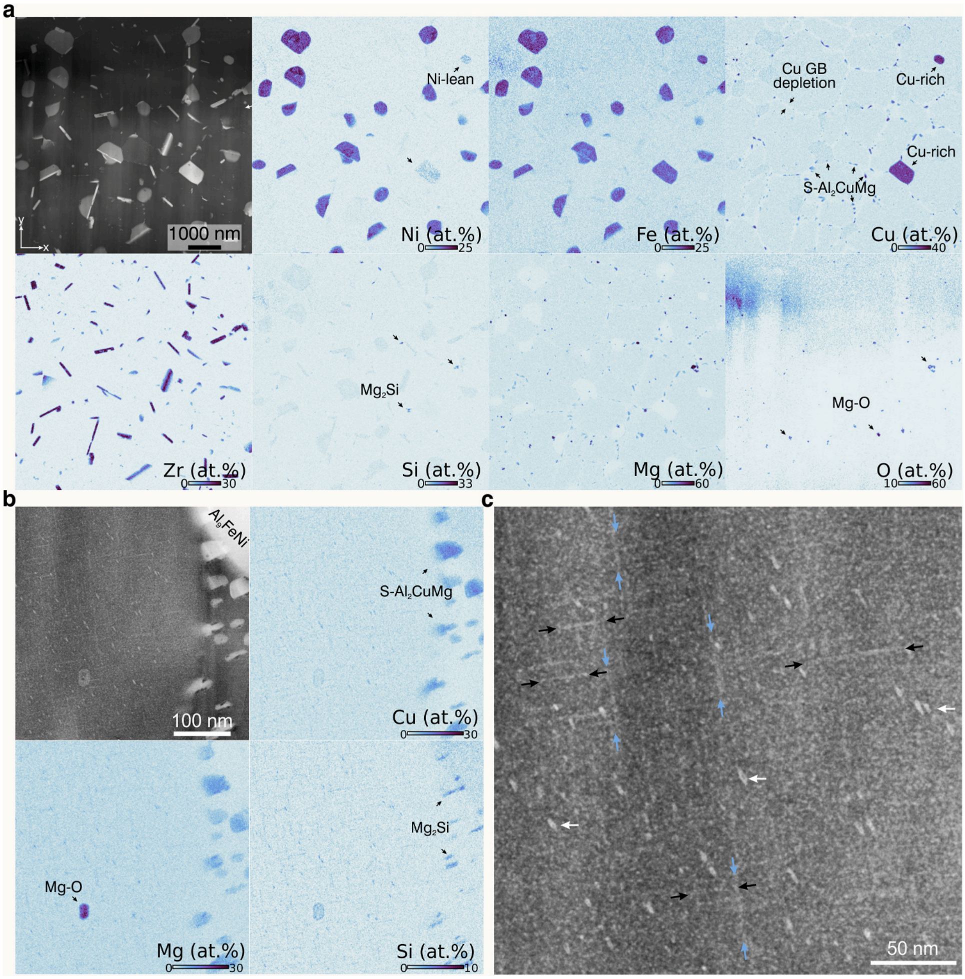

Fig. 6. STEM-EDS of three-step heat-treated sample. a) Numerous D0$_{23}$-Al$_3$Zr rods are visible. Coarse blocky Al$_9$FeNi, as well as Al$_7$Cu$_2$Fe rich precipitates, are located on the Cu-depleted GBs, and smaller S-Al$_2$CuMg precipitates are located in between. b) Close-up of a GB shows Mg-O-rich phases (spinel) within the grain as well as Mg$_2$Si and S-Al$_2$CuMg on the GBs. c) In addition to a large number of nanometric L1$_2$-Al$_3$Zr precipitates, S-Al$_2$CuMg rods are revealed in three orientations within the grain, marked by colored arrows. White arrows mark S-Al$_2$CuMg oriented near-parallel to the electron beam.

number density of these Fe-Ni-rich phases populate the GBs. A large number of rod-shaped, Zr-rich precipitates can be observed on the GBs and within grains of the outer melt pool regions. These appear in two morphologies: 1) as coarse, 0.5–2 µm long and 150–250 nm wide and 2) as fine, 150–500 nm long and 40–50 nm wide precipitates. Along the GBs of the columnar-dendritic region, the Fe-Ni-Cu-rich film has segmented as the result of the annealing, transforming into 50–100 nm wide and 200–600 nm long precipitates. Si-rich precipitates are visible throughout the microstructure.

The subsequent solution annealing step aims at dissolving Cu-Mg-rich phases, which are then available for the formation of nanometric S-Al$_2$CuMg during the final aging step. Solution annealing explicitly refers only to the dissolution of the Cu-Mg-rich phases and not to the Al$_3$Zr precipitates, which only dissolve at temperatures above the liquidus temperature of the matrix. During the solutionizing heat treatment at 530 °C for 1–6 h, the microhardness is significantly reduced compared to the 400 °C 8 h heat-treated condition (Fig. 4). After 1 h at 530 °C, the microhardness drops from 1694 ± 59 MPa to 1357 ± 49 MPa. After 6 h, the microhardness further decreases to 1266 ± 16 MPa. Therefore, a duration of 1 h at 530 °C for the second heat treatment step of solutionizing was chosen for the subsequent experiments, as it is expected to provide sufficient solutionizing with a reduced risk of overaging and grain coarsening, in particular with regard to the targeted L1$_2$-Al$_3$Zr formed in the material during the 400 °C step [32]. Secondary phases are homogeneously distributed in the microstructure (Fig. 5b). The segmented, probably Fe-Ni-rich film on the GBs further agglomerates to form clusters of spheroidized precipitates 350–800 nm in diameter, located notably at triple GB junctions, with the largest fraction of GB area being precipitate-free. Furthermore, blocky, presumably Cu-Fe-rich precipitates of 0.2–1.2 µm edge length are found on the GBs. Due to the metastable state after solutionizing and the imperative subsequent isothermal aging step, a more in-depth characterization of these large precipitates was not performed at this stage, as their identification is to be performed after the final heat treatment step.

In the final artificial aging step at 180 °C, an increase in microhardness from 1357 ± 49 MPa, after solution heat treatment, to 1640 ± 41 MPa is already evident after a duration of only 1 h (Fig. 4). The peak hardness for the investigated heat treatment durations of 1–10 h is reached after 3 h at 1706 ± 35 MPa. A second microhardness maximum at 1635 ± 30 MPa is reached after 6 h, which is, however, lower than the peak hardness. Longer aging durations tend to reduce the hardness, hence 3 h was chosen as the favorable duration for further investigations and will be investigated in detail in the further course. After the last heat treatment step, multiple different precipitates can be detected via SEM-BSD (Fig. 5c) and STEM-EDS imaging (Fig. 6). In addition to 50–100 nm wide, and 300–600 nm long D0$_{23}$-Al$_3$Zr phases, two types of blocky precipitates can be identified: 0.5–1.0 µm sized phases with an equiatomic Fe:Ni ratio and a proposed composition of Al$_9$FeNi, and a 0.5–2.0 µm sized phase with a Cu:Fe atomic ratio of 2:1 and a proposed composition of Al$_7$Cu$_2$Fe, which displays minor Cu (~2.5 at%) and Ni (~4 at%) solubilities, respectively (Figs. 6a, S2, S3). Al$_7$Cu$_2$Fe are observed less frequently than Al$_9$FeNi, with the latter being 10 times more prevalent. The size of the Al$_9$FeNi precipitates increased significantly compared to the first heat treatment step. Sporadically, cuboid-shaped L1$_2$-Al$_3$Zr primary precipitates are observed within the grains. Furthermore, scattered 100–250 nm long and 50–100 nm wide

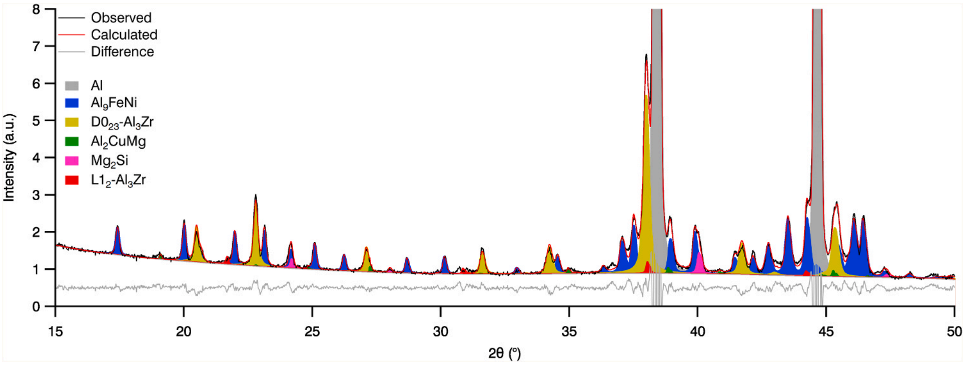

Fig. 7. XRD measurement. Phase identification after Rietveld refinement shows the presence of seven different phases after 400 °C, 8 h + 530 °C, 1 h + 180 °C, 3 h. The phases are quantified as follows (in wt%): Al_9FeNi= 8.84, $D0_{23}$-Al_3Zr= 3.05, Mg_2Si= 1.99, Al_7Cu_2Fe= 1.73, Al_2CuMg= 0.32, $L1_2$-Al_3Zr= 0.14.

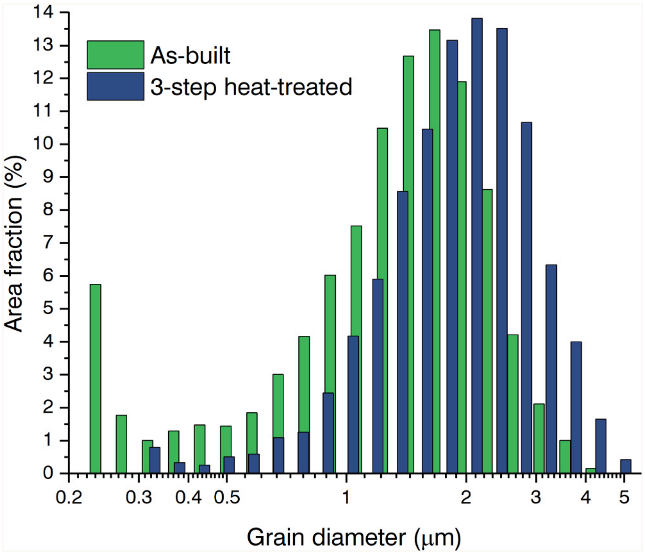

Fig. 8. Grain size distribution before and after the three-stage heat treatment. After the three-stage heat treatment (400 °C, 8 h + 530 °C, 1 h + 180 °C, 3 h), the consumption of fine grains < 0.3 µm on the one hand, and an increase of the mean grain diameter from 1.46 µm in the as-built condition to 2.01 µm in the heat-treated condition on the other hand, are evident.

precipitates with an equiatomic Cu:Mg ratio and a proposed composition of Al_2CuMg can be found on the GBs (Fig. 6a,b). Moreover, Mg-O-rich (spinel) and Mg_2Si precipitates can be detected. Interestingly, Cu-depleted regions are observed along the GBs. A small amount of Sn can be detected in all precipitates. HR-STEM studies allow the identification of two species of nanometric precipitates for the three-step heat-treated samples: 1) A very large number density of spherical, 1–3 nm diameter precipitates, finely distributed within grains. While the STEM-EDS map was not able to reveal localized Zr enrichment due to the nanoprecipitates' extremely small sizes, high number density, and EDS background level, these nanoprecipitates are suspected to be the desired $L1_2$-Al_3Zr [20]. 2) 1–2 nm wide, 10–30 nm long Cu-Mg rich rods, which have formed in between the Zr-rich precipitates (Fig. 6c). A line spectrum perpendicular through these rod precipitates shows an equiatomic ratio of Cu:Mg, suggesting the targeted nanometric S-Al_2CuMg phase. Mg shows pronounced segregation at the interfaces of $D0_{23}$-Al_3Zr as well as Al_9FeNi to the matrix (Fig. S2). Mg_2Si segregation is observed at the interface of larger S-Al_2CuMg on the GBs with the matrix. An increase in Si concentration is also observed, co-localized with the rod-shaped nanometric S-Al_2CuMg; it was, however, not possible to determine if interfacial Mg_2Si is formed or if Si is in solubility within the S-phase. The phases identified by TEM are confirmed and quantified by XRD measurements, revealing seven distinct phases (Fig. 7). Besides the Al matrix, mainly Al_9FeNi is present with a share of 8.8 wt%. The two phases containing Al and Cu, Al_7Cu_2Fe and Al_2CuMg, are quantified at 1.7 wt% and 0.3 wt%, respectively. In addition, 3.0 wt% of $D0_{23}$-Al_3Zr and 0.1 wt% of $L1_2$-Al_3Zr are detected. Beyond that, a share of 2.0 wt% Mg_2Si can be determined. The grain growth suspected from the SEM images is confirmed by EBSD measurements, which show that the average grain size has increased from 1.46 µm to 2.01 µm after a three-step heat treatment (Fig. 8). Melt pool contours are no longer visible, with only isolated fine-grained regions (grain diameter < 500 nm) left, while the majority of the grains have coalesced.

To highlight the need to perform a three-step heat treatment compared to a conventional T6 heat treatment, a two-step heat treatment, consisting of solutionizing at 530 °C for 1 h and subsequent artificial aging for 1–5 h at 180 °C, was carried out, with a particular focus on the difference in mechanical properties (Table 2). Within this T6 heat treatment, the peak microhardness is reached after 3 h of aging, equivalent to the three-step heat treatment (Fig. 4). The microhardness reaches 1635 ± 34 MPa, which is thus 4% lower by 71 MPa. The grain size averages 1.60 µm, which is smaller than that of the three-stage heat-treated sample.

4.3. Mechanical properties

Specimens fabricated parallel to the build direction ("vertical") and perpendicular to the build direction ("horizontal") were tested after various heat treatments to investigate the effect of heat treatment and orientation on mechanical properties. Despite the low material texture (Fig. 5), significantly different mechanical properties are obtained between the different heat-treatment conditions and their build orientation. In general, the vertically oriented specimens show lower elongation to fracture and UTS than the horizontally oriented specimens (Fig. 9a). Furthermore, a serrated stress-strain curve can be observed for all the T6 and three-stage heat-treated samples. Young's modulus of all tested specimens is similar and averages 67.2 ± 0.9 GPa.

The vertical specimens in the as-built and 400 °C configurations show a typical brittle fracture behavior with very low ductile deformation, leading to UTS and elongation to fracture of 427 ± 29 MPa and 448 ± 4 MPa as well as 0.8 ± 0.1% and 0.8 ± 0.1%, respectively. The vertical T6 and three-stage heat-treated specimens show no upper yield point in contrast to the as-built and 400 °C condition, with UTS and elongation to fracture of 387 ± 7 MPa and 2.7 ± 0.6% for the T6 and 378 ± 11 MPa as well as 1.8 ± 0.9% for the three-stage heat treatment. Lack-of-fusion defects with unmelted powder sintered to the inside are often visible on the fracture surfaces (Fig. 10b).

The horizontal as-built specimens show the highest UTS value of all tested samples of 495 ± 3 MPa with an elongation to fracture of 6.1 ± 3.7%, thus displaying the highest standard deviation. However, it is noted that the as-built samples had to be stored at RT for one month due

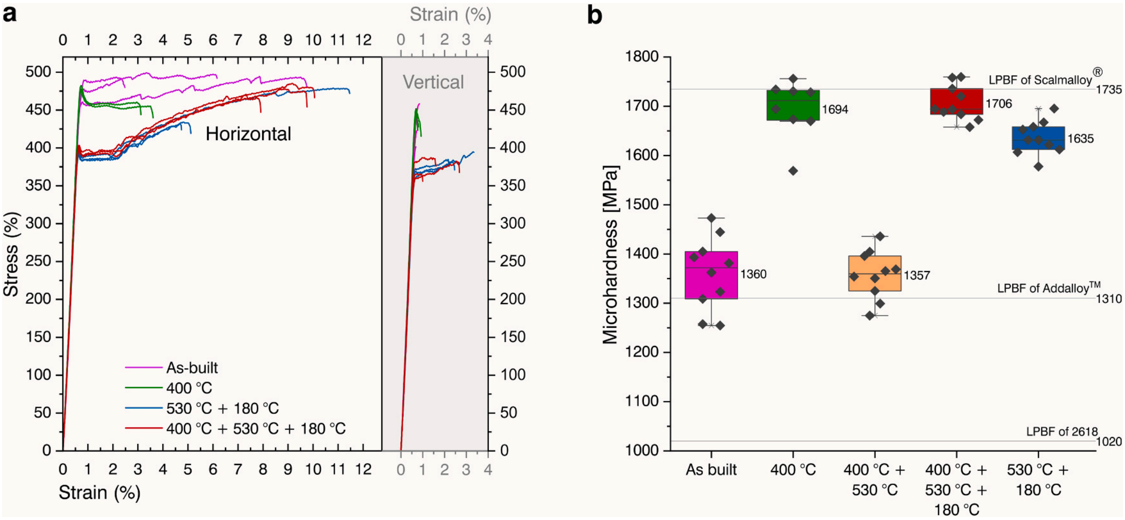

Fig. 9. RT tensile testing and microhardness after different heat treatment stages. a) Specimens manufactured perpendicular ("horizontal") to the build direction exhibit higher mechanical properties than specimens manufactured parallel ("vertical") to the build direction. The as-built tensile samples have been subject to natural aging for one month, leading to potentially overestimated strength. b) Precipitation hardening leads to a significant hardness increase after 400 °C, which drops sharply after solution annealing. Subsequent artificial aging at 180 °C leads to another substantial hardness increase due to the formation of secondary precipitates. T6 heat treatment (530 °C + 180 °C) results in lower hardness values. Reference hardness values refer to heat-treated specimens [16,21,44].

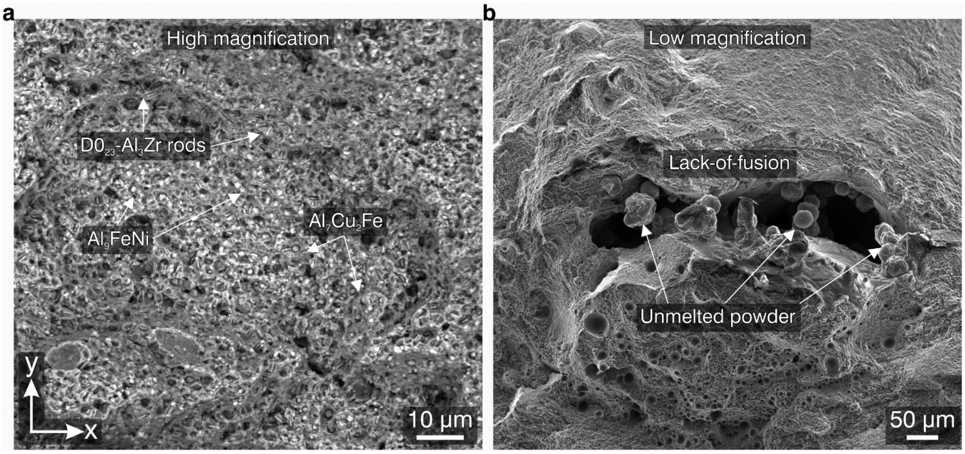

Fig. 10. Fracture surface. a) The X-Y fracture surface of the heat-treated specimens (here exemplary after 400 °C, horizontal) reveal numerous bare precipitates, enclosed by a porous fracture surface morphology. b) Lack-of-fusion defects are visible on the fracture surface, which, due to their orientation perpendicular to the loading direction, have a detrimental effect, especially on the mechanical properties of the vertical tensile test specimens.

to delays in sample manufacturing. The high mechanical properties are thus arising thanks to the natural aging propensity of this class of alloy [42,43], and thus do not truly represent "as-built properties". A comparably high standard deviation can be observed for the T6 heat-treated sample, which displays a UTS of 448 ± 27 MPa and elongation to fracture of 7.1 ± 3.8%. These comparably high standard deviations for the T6 and as-built condition result from outliers (Fig. 9a). The overall highest elongation to fracture values are obtained for the three-step heat-treated specimens with 9.2 ± 1.1%, while showing the second highest UTS of 478 ± 7 MPa. While strain hardening of the as-built and 400 °C specimens is hardly noticeable, it is pronounced in the multistage heat-treated specimens. The overall highest elongation to fracture values are obtained for the three-step heat-treated specimens with 9.2 ± 1.1%. All horizontal specimens exhibit a pronounced yield point, which is most evident in the 400 °C heat-treated specimens and lowest in the as-built specimen.

Fracture surface observations of the horizontally and vertically oriented, 400 °C heat-treated specimens reveal rod-shaped as well as block-shaped precipitates, present within honeycomb-shaped cavities formed during fracture (Fig. 10a). For the as-built conditions, those are absent, while for the T6 and three-stage heat-treated conditions, they are only slightly evident (Fig. S4).

Table 3
Mechanical properties of different heat treatment conditions and build-up orientations. AB: As-built. 1 S: 400 °C, 8 h. 3 S: 400 °C, 8 h + 530 °C, 1 h + 180 °C, 3 h. T6: 530 °C, 1 h + 180 °C, 3 h.

Condition	Build-up orientation	Young's modulus (GPa)	$R_{p0.2}$ (MPa)	UTS (MPa)	Elongation (%)
AB	Horizontal	66.6 ± 0.5	476 ± 14	495 ± 3	6.1 ± 3.7
1 S	Horizontal	68.4 ± 0.6	479 ± 3	479 ± 3	2.5 ± 1.5
3 S	Horizontal	67.1 ± 0.8	401 ± 3	478 ± 7	9.2 ± 1.1
T6	Horizontal	67.5 ± 1.5	392 ± 2	448 ± 27	7.1 ± 3.8
AB	Vertical	68.1 ± 1.9	427 ± 29	427 ± 29	0.8 ± 0.1
1 S	Vertical	67.8 ± 0.4	448 ± 4	448 ± 4	0.8 ± 0.1
3 S	Vertical	66.1 ± 1.8	369 ± 11	378 ± 11	1.8 ± 0.9
T6	Vertical	66.3 ± 1.5	367 ± 5	387 ± 7	2.7 ± 0.6

It is noteworthy that many specimens fractured outside the measuring range of the extensometer. Therefore, the machine displacement records were calibrated to determine the strain evolution until rupture (Supplementary material). The obtained mechanical properties are summarized in Table 3.

5. Discussion

5.1. High-temperature aging at 400 °C

The first heat treatment step at 400 °C for 8 h aims at forming a high number density of nm-sized secondary L1$_2$-Al$_3$Zr, which can contribute to a high degree of precipitation hardening when homogeneously dispersed in the matrix [16,45]. This heat treatment step was only performed within the three-step heat treatment (Table 2). The process-inherent rapid solidification in LPBF provides a high level of Zr supersaturation in the Al matrix, which is then available for precipitate formation after heat treatment. Based on microhardness measurements, the peak hardness of 1695 ± 59 MPa is achieved after a holding time of 8 h (Fig. 9b), which is in agreement with previous studies on Zr-modified Al-Mg and Al-Cu-Mg alloys [16,32]. This L1$_2$-Al$_3$Zr induced strengthening is extremely potent, as evidenced by the microhardness increase of 1360 ± 74 MPa to 1695 ± 59 MPa, an increase of 25% (Fig. 4).

Already after this period, a considerable fraction of the stable D0$_{23}$-Al$_3$Zr phase, which is typically not desired due to the lower precipitation-hardening effect based on its incoherence and size, is formed from the metastable primary L1$_2$-Al$_3$Zr phase. Although the latter is characterized by its excellent high-temperature stability due to the low lattice mismatch between L1$_2$ and Al of 0.52% and the low diffusion rate of Zr at $2.26 \cdot 10^{-21}$ m^2/s^{-1} at 400 °C, the early observation of D0$_{23}$ can be explained by the known acceleration of the L1$_2$ → D0$_{23}$ phase transformation in the presence of Cu, originating from reduced kinetic stability of L1$_2$ with increasing Cu content [19,46,47]. However, due to their comparably small size of 150–500 nm length and 40–50 nm width, as well as the overall high phase fraction (estimated at 3.0 wt% by XRD), these fine D0$_{23}$ needles are likewise expected to contribute to a minor degree to the hardness increase. For longer heat treatment durations at 400 °C, the microhardness tends to decrease progressively (Fig. 9b). The primary reason for this is the concomitant growth of the L1$_2$-Al$_3$Zr and their phase transformation to D0$_{23}$. In turn, reducing the volume fraction and coarsening of the desired L1$_2$ phase leads to an overall decrease in the effectiveness of precipitation hardening.

An additional mechanism that can explain the decreasing microhardness is associated with a by-product of annealing at 400 °C: the progressive segmentation and agglomeration of the as-built continuous film on the GBs, presumably consisting of Al$_9$FeNi and Al$_2$CuMg based on ThermoCalc® calculations (Fig. 3). Due to the segmentation of the GB film as well as grain growth, the grains are located directly adjacent to each other, which allows stress fields and associated dislocation generation to start in neighboring grains more easily than across a GB film. The segmented precipitates are predominantly Al$_9$FeNi according to the Thermo-Calc® calculations, since Al$_2$CuMg dissolves at 263 °C and Al$_9$FeNi is stable up to 623 °C (Fig. 3). Moreover, a blocky phase is formed on the GBs, which is assumed to be Al$_7$Cu$_2$Fe according to the Thermo-Calc® calculations. The high ratio of alloying elements in solution in the as-built state after rapid solidification and the dissolution of Al$_2$CuMg during this step enable the formation of this phase [48].

5.2. Solutionizing at 530 °C

This heat treatment step aims at dissolving Cu- and Mg-rich compounds and bringing them into solution in the matrix so that they are available for the formation of the nm-sized S-Al$_2$CuMg rods. It represents the second step of the three-step heat treatment and, equally, the first step of the T6 heat treatment (Table 2).

According to the Thermo-Calc® calculations (Fig. 3), 1 wt% Al$_7$Cu$_2$Fe dissolves at 530 °C, while Mg$_2$Si fully dissolves simultaneously. Previous studies have shown that a continuous eutectic film on the GBs, as it is present in the as-built and also still after 400 °C, can suppress grain growth [32]. The dissolution of this film leads to the significant reduction of the fine-grained regions at the melt pool boundaries (Fig. 5b). This explains the slightly stronger texture in the heat-treated condition compared to the as-built condition, as the comparatively coarse columnar-dendritic grains coalesce with the fine-equiaxed grains and increase in size. Moreover, the Al$_9$FeNi phase grows and leaves precipitation-free intermediate GBs, except for triple junction points (Fig. 5b). The depletion of solutes (mainly Cu and Mg) along the GBs during the solution heat treatment and, to a smaller extent, through pipe diffusion in the final aging step, leads to precipitate-free-zones (PFZ) along the GBs and the formation of precipitates at different preferential sites. The width of the PFZ is determined by the diffusion rate of the solute atoms to *intra*granular precipitates and the potency to form and grow *inter*granular precipitates in the matrix phase [49]. The formation of *intra*granular precipitates is – according to classical nucleation theory – determined by the boundary energy, which is maximized at triple GB junctions [37]. This leads to the precipitation of mainly Al$_9$FeNi at triple points, which are thermodynamically stable at 530 °C (Fig. 5b); their presence can then hinder the GB movement and control the grain growth [37]. In conventionally fabricated 2618, which is strengthened by a T6 heat treatment, initial breakup, then segmentation, and progressive reduction of the continuous GB film can be observed with increasing solution annealing time in a similar manner [50]. While the solution heat treatment duration of a T6 heat treatment typically involves holding times of 8–16 h [34,51], the dissolution of the relevant phases can be achieved in 1 h in LPBF material because of the reduced phase sizes. Due to the short holding time of 1 h, overaging of the L1$_2$-Al$_3$Zr is kept to a minimum as evidenced by their small radii even after the three-step treatment, although further nucleation of L1$_2$, as well as transformation into D0$_{23}$ cannot be excluded either, which in turn affects the associated strengthening effect.

5.3. Low-temperature aging at 180 °C

The final heat treatment step aims at the formation of rod-shaped, nm-sized S-Al$_2$CuMg precipitates within the grains. This is enabled by the previous solution annealing, aiming at dissolving the highest concentration of Cu and Mg as possible into the Al matrix. In many 2xxx series alloys, especially in 2618, S-Al$_2$CuMg is the main strength-enhancing phase. The increase in microhardness from 1357 ± 49 MPa to 1706 ± 35 MPa for the three-step heat treatment and the more modest increase from 1355 ± 40 MPa to 1635 ± 34 MPa for the T6 heat treatment, which represent an increase of hardness of 26% and 20%, respectively, can be attributed primarily to the precipitation of this phase (Fig. 9b). In conventionally produced and T6 heat-treated 2618, Al$_9$FeNi, Mg$_2$Si, and Al$_2$Cu exist in addition. In the case of a non-optimal ratio of Fe:Ni‡ 1 (wt%), Ni and Fe are not entirely bound within Al$_9$FeNi (whose exact stoichiometry is Al$_9$Fe$_{0.7}$Ni$_{1.2}$) but either Al$_7$Cu$_2$Fe or AlCuNi are formed, depending on the predominant element [37]. The typical phases observed in conventionally produced and heat-treated 2618 could also be identified by XRD measurement in the LPBF material, in addition to Al$_3$Zr (metastable L1$_2$ as well as stable D0$_{23}$).

Al$_9$FeNi has by far the largest fraction of all secondary phases (8.8 wt %). Directly adjacent to Al$_9$FeNi, D0$_{23}$-Al$_3$Zr are often formed by interfacial precipitation, with a small amount of Sn and Si dissolved in D0$_{23}$. In addition to Mg being found in S-Al$_2$CuMg, Mg is also present as spinel, MgAl$_2$O$_4$, as well as in Mg$_2$Si on the GBs. The large width of the Mg$_2$Si peak in the XRD spectrum suggests that this phase is nanometric in size. Although a large amount of Fe is bound within the Al$_9$FeNi intermetallics, the Fe:Ni ratio of the alloy of 1.2 indicates that excess Fe is available for the formation of Al$_7$Cu$_2$Fe intermetallics, localized on GBs, with a phase fraction estimated from XRD of 1.7 wt%. The formation of this phase is undesirable as it binds Cu, which is therefore available to a lesser extent for the formation of the targeted nanometric S-Al_2CuMg. HR-STEM reveals S-Al_2CuMg rods measuring 30–100 nm in length and 1–3 nm in diameter within the grains. As S'', S', and S are crystallographically identical and differ only in the degree of coherency to Al and slightly different strains, no distinction between these configurations is made in this work; however, the S configuration is to be expected as the overaged type, with S'' and S′ being transient phases [52]. In addition to the nanometric S-Al_2CuMg, coarser, blocky S-Al_2CuMg with a size of 50–150 nm is evident on the GBs, formed by pipe diffusion of Cu and Mg. GBs serve as very efficient vacancy sinks, allowing solute atoms within the grains to diffuse across the vacancy mechanism and form intergranular precipitates, in particular the S-Al_2CuMg on GBs [49]. This is evidenced by the ~35 nm wide zone close to the GBs depleted of nano S-Al_2CuMg.

It is yet unclear whether the $L1_2$-Al_3Zr formed in the first step can act as nucleation sites for the formation of the nanometric S-Al_2CuMg rods, as has already been shown in the literature for conventionally manufactured, Zr-modified 2618 [51,53]. For LPBF-manufactured Al alloys, which contain significantly more Zr (and often Sc), this effect has not yet been demonstrated. Contrary to this, it is also possible that the high number of nm-sized $L1_2$-Al_3Zr formed in the first step could hinder the growth of the S-Al_2CuMg needles. A high volume fraction of the strength-enhancing $L1_2$-Al_3Zr precipitates, formed presumably after the first heat treatment step, can be detected within the grains. The $L1_2$-Al_3Zr precipitates are underaged, with a diameter of 1–3 nm, compared to a more ideal diameter of 3–5 nm to achieve maximum strengthening for the current volume fraction based on literature [54]. Makineni et al. demonstrated that these $L1_2$-Al_3Zr can serve as nucleation seeds for θ'-Al_2Cu in Al-Cu alloys containing 0.15 wt% Zr, thus refining θ'-Al_2Cu and increasing its number density [45]. The same phenomenon is suspected to similarly promote the heterogeneous nucleation of the nm-sized S-Al_2CuMg rods. However, due to the significantly higher amount of Zr in our alloy (1.7 wt%), which induces a higher volume fraction of nm-sized $L1_2$-Al_3Zr, the number density of $L1_2$-Al_3Zr nano-precipitates may act as obstacles to the more numerous rod-shaped S-Al_2CuMg that are heterogeneously nucleated. Additionally, while increasing Zr contents are accompanied by increasing strength for 5xxx alloys, the phase transformation from metastable $L1_2$ to stable $D0_{23}$ – facilitated by Cu – has to be considered a priori when designing an alloy exposed to multi-stage heat treatments [16,46].

5.4. Mechanical properties after various heat treatment steps

The mechanical properties were assessed by uniaxial tensile tests on differently heat-treated specimens of different orientation, thus manufactured parallel ("vertical") and orthogonal ("horizontal") to the build-up direction. The vertical specimens show overall lower mechanical properties in the plastic region, compared to their horizontally fabricated counterparts (Fig. 9a). This correlation is known from literature for samples displaying lack-of-fusion defects [55], which can be distinctly identified by the unmelted powder particles sintered to the defects' surfaces (Fig. 10b). For the vertical specimens, those defects are oriented perpendicular to the loading direction and cause high stress concentrations [56]. Due to their orientation, they have a significantly more detrimental effect on vertical than on horizontal specimens.

The formation of these lack-of-fusion defects is attributed to a certain degradation of the powder over time during storage in the laboratory for approximately one year. Since the alloy contains – besides Al – relatively high amounts of the reactive elements Zr and Mg, this is probably due to a reaction with oxygen from the atmosphere, even though the powder was stored in closed vessels containing silica gel bags. The correlation of lower tensile test properties due to powder aging has recently been proven for LPBF and DMD of AlSi10Mg [40,41,57]. A more detailed study on the influence of storage conditions and storage time on the degradation of Zr-containing Al alloys is currently in progress.

After manufacturing the samples and in the course of the performed heat treatments, several effects on microstructure, precipitation formation, and consequently on the mechanical properties can be observed. The as-built samples show excellent values for $R_{p0.2}$ and UTS with 476 ± 14 MPa and 495 ± 3 MPa, respectively, which can be attributed to the potent natural aging due to the samples' exposure to RT for about a month [42]. Since the microhardness measurements were performed on fresh samples within a very short time after production, the measured values of microhardness and $R_{p0.2}$ thus differ significantly. After LPBF, direct aging (natural or artificial) is a common procedure, as the very rapid solidification squeezes atoms into solid solution, which are then available for the formation of precipitates [42]. Notably, in the course of the artificial heat treatment, and especially after the low-temperature precipitation aging step, the effect of natural aging becomes negligible. The prevailing strengthening mechanism of natural aging in Al-Cu alloys is based on the formation of Cu-Mg clusters and GP-zones, not on S-phase formation as in T6 heat-treated samples [58], as the GP-zones are unstable at higher temperatures. The presence of small amounts of Mg massively accelerates the formation of these clusters [59].

The typically high dislocation density in the as-built samples prevents further strain hardening, accounting for the very low increase of the stress-strain curve in the plastic regime due to predominant dynamic recovery effects [60]. Nevertheless, the very fine-grained microstructure (average grain size 1.46 μm) causes both high strength and ductility. The increase in ductility can be explained by the increased probability of a moving dislocation encountering a suitably oriented adjacent grain when crossing a GB (slip plane lies in the direction of shear stress). The vertically manufactured specimens show brittle fracture, with the crack located at the site of radial cross-sectional increase outside the gauge length. This can be attributed to an increased notch sensitivity associated with the lower ductility, as this region functions as a shallow notch [61].

The specimens subjected to a heat treatment at 400 °C exhibit mechanical properties comparable to the as-built specimens but with a lower elongation to fracture, particularly in the case of the horizontally-oriented specimens. Considering the positive effect of $L1_2$-Al_3Zr precipitation hardening on YS and UTS demonstrated in the Zr-modified 5xxx Al-Mg alloy Addalloy™ after 8 h at 400 °C [16], it is reasonable to assume a similar positive effect of the heat treatment on the mechanical properties of our specimens. However, it can be inferred that this effect would have been more pronounced without prior natural aging. This emphasizes the significant potential of precipitation strengthening in Al-Cu alloys but also underscores the importance of careful part handling to consider the effects of natural aging during processing. The UTS of the horizontally-oriented specimens, which is identical to the upper YS, is comparable to that of the multistage heat-treated specimens and demonstrates a pronounced YS. This phenomenon is attributed to the diffusion of Mg towards energetically favorable elastic stress fields of dislocations. To initiate plastic deformation, dislocations must separate from the Mg-Cotrell cloud formed around them, enabling their movement along the slip plane at lower stress levels [62]. While this underlying mechanism is well-established for low carbon steels and Al-Mg alloys, it has not yet been discussed in the context of LPBF-fabricated Al-Cu-Mg alloys [44,48]. Despite the high strength achieved after the 400 °C treatment, the ductility remains poor, likely due to the presence of a high fraction of brittle phases that require solutionization.

For the multistage heat-treated samples, the Cotrell effect is much less pronounced, since the Mg concentration remaining in solid solution is partially consumed to form the strengthening S-Al_2CuMg precipitates (within the grains and on the GBs). These samples show significant strain hardening due to the nm-sized $L1_2$-Al_3Zr as well as S-Al_2CuMg within grains, which effectively impede the dislocation motion.

The three-step treatment, when compared to the classical T6 heat treatment, demonstrates superior mechanical properties in terms of

Table 4
Comparison of mechanical properties of the investigated 2618 +Zr alloy with literature data of various Zr-modified and 2xxx series alloys, manufactured by LPBF as well as conventionally by forging and casting. Where indicated, the data given refer to specimens set up parallel to the build platform ("horizontal").

	Composition	Condition	Microhardness (MPa)	Fracture strain (%)	YS/$R_{p0.2}$ (MPa)	UTS (MPa)	Source
LPBF	2618 +Zr	As-built	1360 ± 74	6.1 ± 3.7	476 ± 14	495 ± 3	[This work]
		400 °C + T6	1706 ± 35	9.2 ± 1.1	401 ± 3	478 ± 7	
		T6	1635 ± 34	7.1 ± 3.8	392 ± 2	448 ± 27	
	2618	As-built	1020	-	211 ± 4	-	[44]
		T6	1302	-	316 ± 5	-	
	Addalloy™	As-built	961 ± 33	25.2 ± 1.6	290 ± 6	329 ± 3	[16]
		400 °C	1310 ± 42	23.9 ± 4.4	365 ± 11	389 ± 4	
	AlCuMgZr	As-built	1099 ± 44	-	-	-	[32]
		400 °C + T6	1409 ± 23	-	339 ± 9	-	
	2024 +Zr	As-built	-	14.1 ± 1.6	376 ± 7	441 ± 7	[29]
		T6	-	6.9 ± 1.8	402 ± 9	483 ± 37	
Cast/ Forged	2618	As-cast	735	8	121	200	[35]
		T61 (forged)	-	10	370	440	[64]
	2024	As-cast	785	12	75	185	[65]
		T6 (forged)	1324	10	393	476	

microhardness, elongation to fracture, YS, and UTS, emphasizing the advantages of including a 400 °C aging step to promote the formation of nm-sized $L1_2$-Al_3Zr precipitates in Zr-modified 2xxx series alloys (Table 4). However, it is worth noting that the two-stage T6 heat treatment, which excludes this high-temperature aging step, results in less grain growth of the Al matrix, which could have a positive impact on microhardness, elongation to fracture, YS, and UTS. Nevertheless, lower microhardness values (Fig. 9b) and the presence of high standard deviations in the mechanical properties, attributed to a significant outlier (Fig. 9a), are observed. Consequently, it can be concluded that the precipitation formation achieved through the two-stage heat treatment is inferior to that of the three-stage heat treatment.

To achieve the optimal formation of strength-enhancing precipitates in both heat treatment variants, it is necessary to consider contrasting effects. On one hand, an additional high-temperature aging step may result in the overaging of metastable $L1_2$-Al_3Zr or even a transformation to stable $D0_{23}$-Al_3Zr, particularly favored by the presence of Cu [46]. On the other hand, the absence of this step carries the risk of suboptimal number density, volumetric distribution, and size of the $L1_2$-Al_3Zr precipitates. Considering the considerations related to precipitate formation and the observed mechanical properties, it is reasonable to hypothesize that the three-step heat treatment surpasses the standard T6 treatment.

The modified alloy exhibits similar mechanical properties to a T61 heat-treated conventional 2618 but slightly exceeds them in terms of YS and UTS, thus meeting industrial standards [63]. Compared to other LPBF Al alloys, our Zr-modified 2618 shows comparable tensile strength to a Zr-modified 2024 [29], and higher YS and UTS than the commercial Zr-modified 5xxx series Addalloy™, which, however, comes at the cost of ductility, with Addalloy™ having a 2.6 times higher elongation to fracture [16].

6. Conclusions

This work investigates the microstructure and mechanical properties of a Zr-modified 2618 aluminum alloy, adapted to the LPBF process, after various stages of tailored heat treatment. To exploit the full potential of precipitation hardening alloys containing Zr, the heat treatment must be adapted to the microstructures and phases present in the as-built as well as the corresponding heat treatment stages to achieve optimized mechanical properties. During the course of the designed three-step heat treatment, a dual population of nanometer-sized $L1_2$-Al_3Zr and S-Al_2CuMg precipitates are formed which strengthen the alloy. The knowledge gained can promote the development of novel age-hardenable aluminum alloys with improved mechanical properties, bridging the gap toward more commercially available alloys tailored to LPBF. In particular, the following conclusions were reached:

- Finely dispersed, nanometer-sized $L1_2$-Al_3Zr, as well as S-Al_2CuMg, are dispersed within the grains and provide strength to the material.
- Significant amounts of stable $D0_{23}$-Al_3Zr, as well as Al_7Cu_2Fe, can be identified. No Al_2Cu, known from cast 2618, is observed.
- The alloy exhibits a UTS of 478 ± 7 MPa, YS of 401 ± 3 MPa, and elongation to fracture of 9.2 ± 1.1% after three-step heat treatment, matching industry-standard values of cast heat-treated 2618. A microhardness of 1706 ± 35 MPa is achieved.
- Three-step heat treatment is not only preferable to conventional T6 in terms of mechanical properties but also takes better advantage of the positive effects of the Zr addition.

CRediT authorship contribution statement

Marvin Schuster: Conceptualization, Methodology, Investigation, Validation, Formal analysis, Visualization, Writing – original draft. **Anthony De Luca:** Conceptualization, Methodology, Investigation, Visualization, Writing – review & editing, Supervision. **Dagmara Kucajda:** Investigation. **Ehsan Hosseini:** Investigation, Formal analysis, Writing – review & editing. **Remo Widmer:** Investigation, Formal analysis, Writing – review & editing. **Xavier Maeder:** Investigation. **Christian Leinenbach:** Conceptualization, Writing – review & editing, Supervision, Project administration, Funding acquisition.

Declaration of Competing Interest

The authors declare that they have no known competing financial interests or personal relationships that could have appeared to influence the work reported in this paper.

Data availability

Data will be made available on request.

Acknowledgments

The research leading to this work was funded by the Swiss Innovation Agency (Innosuisse) under project Nr. 27436.1 PFNM-NM.

Appendix A. Supporting information

Supplementary data associated with this article can be found in the online version at doi:10.1016/j.jallcom.2023.171166.

References

[1] W.E. Frazier, Metal additive manufacturing: a review, J. Mater. Eng. Perform. 23 (2014) 1917–1928, https://doi.org/10.1007/s11665-014-0958-z.

[2] D. Buchbinder, H. Schleifenbaum, S. Heidrich, W. Meiners, J. Bültmann, High power selective laser melting (HP SLM) of aluminum parts, Phys. Procedia 12 (2011) 271–278, https://doi.org/10.1016/j.phpro.2011.03.035.

[3] X.P. Li, X.J. Wang, M. Saunders, A. Suvorova, L.C. Zhang, Y.J. Liu, M.H. Fang, Z. H. Huang, T.B. Sercombe, A selective laser melting and solution heat treatment refined Al–12Si alloy with a controllable ultrafine eutectic microstructure and 25% tensile ductility, Acta Mater. 95 (2015) 74–82, https://doi.org/10.1016/j.actamat.2015.05.017.

[4] P.A. Hooper, Melt pool temperature and cooling rates in laser powder bed fusion, Addit. Manuf. 22 (2018) 548–559, https://doi.org/10.1016/j.addma.2018.05.032.

[5] A. Aversa, G. Marchese, A. Saboori, E. Bassini, D. Manfredi, S. Biamino, D. Ugues, P. Fino, M. Lombardi, New Aluminum Alloys Specifically Designed for Laser Powder Bed Fusion: A Review, Materials 12 (2019) 1007, https://doi.org/10.3390/ma12071007.

[6] J. Zhang, B. Song, Q. Wei, D. Bourell, Y. Shi, A review of selective laser melting of aluminum alloys: Processing, microstructure, property and developing trends, J. Mater. Sci. Technol. 35 (2019) 270–284, https://doi.org/10.1016/j.jmst.2018.09.004.

[7] N.T. Aboulkhair, M. Simonelli, L. Parry, I. Ashcroft, C. Tuck, R. Hague, 3D printing of Aluminium alloys: Additive Manufacturing of Aluminium alloys using selective laser melting, Prog. Mater. Sci. 106 (2019), 100578, https://doi.org/10.1016/j.pmatsci.2019.100578.

[8] Y. Cao, H.L. Wei, T. Yang, T.T. Liu, W.H. Liao, Printability assessment with porosity and solidification cracking susceptibilities for a high strength aluminum alloy during laser powder bed fusion, Addit. Manuf. 46 (2021), 102103, https://doi.org/10.1016/j.addma.2021.102103.

[9] J.H. Martin, B.D. Yahata, J.M. Hundley, J.A. Mayer, T.A. Schaedler, T.M. Pollock, 3D printing of high-strength aluminium alloys, Nature 549 (2017) 365–369, https://doi.org/10.1038/nature23894.

[10] M.L. Montero-Sistiaga, R. Mertens, B. Vrancken, X. Wang, B. Van Hooreweder, J.-P. Kruth, J. Van Humbeeck, Changing the alloy composition of Al7075 for better processability by selective laser melting, J. Mater. Process. Technol. 238 (2016) 437–445, https://doi.org/10.1016/j.jmatprotec.2016.08.003.

[11] C. Galy, E. Le Guen, E. Lacoste, C. Arvieu, Main defects observed in aluminum alloy parts produced by SLM: From causes to consequences, Addit. Manuf. 22 (2018) 165–175, https://doi.org/10.1016/j.addma.2018.05.005.

[12] L. Zhou, T. Huynh, S. Park, H. Hyer, A. Mehta, S. Song, Y. Bai, B. McWilliams, K. Cho, Y. Sohn, Laser powder bed fusion of Al–10 wt% Ce alloys: microstructure and tensile property, J. Mater. Sci. 55 (2020) 14611–14625, https://doi.org/10.1007/s10853-020-05037-z.

[13] J. Fiocchi, A. Tuissi, C.A. Biffi, Heat treatment of aluminium alloys produced by laser powder bed fusion: A review, Mater. Des. 204 (2021), 109651, https://doi.org/10.1016/j.matdes.2021.109651.

[14] J.T. McKeown, A.K. Kulovits, C. Liu, K. Zweiacker, B.W. Reed, T. LaGrange, J.M. K. Wiezorek, G.H. Campbell, In situ transmission electron microscopy of crystal growth-mode transitions during rapid solidification of a hypoeutectic Al–Cu alloy, Acta Mater. 65 (2014) 56–68, https://doi.org/10.1016/j.actamat.2013.11.046.

[15] J. Damon, R. Koch, D. Kaiser, G. Graf, S. Dietrich, V. Schulze, Process development and impact of intrinsic heat treatment on the mechanical performance of selective laser melted AISI 4140, Addit. Manuf. 28 (2019) 275–284, https://doi.org/10.1016/j.addma.2019.05.012.

[16] J.R. Croteau, S. Griffiths, M.D. Rossell, C. Leinenbach, C. Kenel, V. Jansen, D. N. Seidman, D.C. Dunand, N.Q. Vo, Microstructure and mechanical properties of Al-Mg-Zr alloys processed by selective laser melting, Acta Mater. 153 (2018) 35–44, https://doi.org/10.1016/j.actamat.2018.04.053.

[17] A.B. Spierings, K. Dawson, T. Heeling, P.J. Uggowitzer, R. Schäublin, F. Palm, K. Wegener, Microstructural features of Sc- and Zr-modified Al-Mg alloys processed by selective laser melting, Mater. Des. 115 (2017) 52–63, https://doi.org/10.1016/j.matdes.2016.11.040.

[18] K.E. Knipling, D.C. Dunand, D.N. Seidman, Criteria for developing castable, creep-resistant aluminum-based alloys – A review, MEKU 97 (2006) 246–265, https://doi.org/10.3139/146.101249.

[19] K.E. Knipling, D.C. Dunand, D.N. Seidman, Precipitation evolution in Al–Zr and Al–Zr–Ti alloys during isothermal aging at 375–425°C, Acta Mater. 56 (2008) 114–127, https://doi.org/10.1016/j.actamat.2007.09.004.

[20] S. Griffiths, M.D. Rossell, J. Croteau, N.Q. Vo, D.C. Dunand, C. Leinenbach, Effect of laser rescanning on the grain microstructure of a selective laser melted Al-Mg-Zr alloy, Mater. Charact. (2018), https://doi.org/10.1016/j.matchar.2018.03.033.

[21] K. Schmidtke, F. Palm, A. Hawkins, C. Emmelmann, Process and Mechanical Properties: Applicability of a Scandium modified Al-alloy for Laser Additive Manufacturing, Phys. Procedia 12 (2011) 369–374, https://doi.org/10.1016/j.phpro.2011.03.047.

[22] L. Pantělejev, D. Koutný, D. Paloušek, J. Kaiser, Mechanical and Microstructural Properties of 2618 Al-Alloy Processed by SLM Remelting Strategy, MSF 891 (2017) 343–349, https://doi.org/10.4028/www.scientific.net/MSF.891.343.

[23] S.C. Wang, M.J. Starink, Two types of S phase precipitates in Al–Cu–Mg alloys, Acta Mater. 55 (2007) 933–941, https://doi.org/10.1016/j.actamat.2006.09.015.

[24] B. Ahuja, M. Karg, K.Yu Nagulin, M. Schmidt, Fabrication and characterization of high strength Al-Cu alloys processed using laser beam melting in metal powder bed, Phys. Procedia 56 (2014) 135–146, https://doi.org/10.1016/j.phpro.2014.08.156.

[25] X. Nie, H. Zhang, H. Zhu, Z. Hu, L. Ke, X. Zeng, Analysis of processing parameters and characteristics of selective laser melted high strength Al-Cu-Mg alloys: From single tracks to cubic samples, J. Mater. Process. Technol. 256 (2018) 69–77, https://doi.org/10.1016/j.jmatprotec.2018.01.030.

[26] X. Nie, H. Zhang, H. Zhu, Z. Hu, L. Ke, X. Zeng, Effect of Zr content on formability, microstructure and mechanical properties of selective laser melted Zr modified Al-4.24Cu-1.97Mg-0.56Mn alloys, J. Alloy. Compd. 764 (2018) 977–986, https://doi.org/10.1016/j.jallcom.2018.06.032.

[27] H. Zhang, H. Zhu, X. Nie, J. Yin, Z. Hu, X. Zeng, Effect of Zirconium addition on crack, microstructure and mechanical behavior of selective laser melted Al-Cu-Mg alloy, Scr. Mater. 134 (2017) 6–10, https://doi.org/10.1016/j.scriptamat.2017.02.036.

[28] F. Czerwinski, Thermal stability of aluminum alloys, Materials 13 (2020) 3441, https://doi.org/10.3390/ma13153441.

[29] Y. Wang, X. Lin, N. Kang, Z. Wang, Q. Wang, Y. Liu, W. Huang, Laser powder bed fusion of Zr-modified Al–Cu–Mg alloy: Crack-inhibiting, grain refinement, and mechanical properties, Mater. Sci. Eng.: A (2022), 142618, https://doi.org/10.1016/j.msea.2022.142618.

[30] G. Li, E. Brodu, J. Soete, H. Wei, T. Liu, T. Yang, W. Liao, K. Vanmeensel, Exploiting the rapid solidification potential of laser powder bed fusion in high strength and crack-free Al-Cu-Mg-Mn-Zr alloys, Addit. Manuf. 47 (2021), 102210, https://doi.org/10.1016/j.addma.2021.102210.

[31] M. Schuster, A. De Luca, R. Widmer, X. Maeder, C. Leinenbach, Processability, microstructure and precipitation of a Zr-modified 2618 aluminium alloy fabricated by laser powder bed fusion, J. Alloy. Compd. 913 (2022), 165346, https://doi.org/10.1016/j.jallcom.2022.165346.

[32] M. Schuster, A. De Luca, A. Mathur, E. Hosseini, C. Leinenbach, Precipitation in a 2xxx series Al-Cu-Mg-Zr alloy fabricated by laser powder bed fusion, Mater. Des. 211 (2021), 110131, https://doi.org/10.1016/j.matdes.2021.110131.

[33] M.S. Kenevisi, Y. Yu, F. Lin, A review on additive manufacturing of Al–Cu (2xxx) aluminium alloys, processes and defects, Mater. Sci. Technol. 37 (2021) 805–829, https://doi.org/10.1080/02670836.2021.1958487.

[34] İ. Özbek, A study on the re-solution heat treatment of AA 2618 aluminum alloy, Mater. Charact. 58 (2007) 312–317, https://doi.org/10.1016/j.matchar.2006.07.002.

[35] E.M. Elgallad, P. Shen, Z. Zhang, X.-G. Chen, Effects of heat treatment on the microstructure and mechanical properties of AA2618 DC cast alloy, Mater. Des. 61 (2014) 133–140, https://doi.org/10.1016/j.matdes.2014.04.045.

[36] I.N.A. Oguocha, S. Yannacopoulos, Precipitation and dissolution kinetics in Al–Cu–Mg–Fe–Ni alloy 2618 and Al–alumina particle metal matrix composite, Mater. Sci. Eng.: A 231 (1997) 25–33, https://doi.org/10.1016/S0921-5093(97)00065-8.

[37] F. Nový, M. Janeček, R. Král, Microstructure changes in a 2618 aluminium alloy during ageing and creep, J. Alloy. Compd. 487 (2009) 146–151, https://doi.org/10.1016/j.jallcom.2009.08.014.

[38] A.A. Coelho, TOPAS and TOPAS-Academic: an optimization program integrating computer algebra and crystallographic objects written in C++, J. Appl. Cryst. 51 (2018) 210–218, https://doi.org/10.1107/S1600576718000183.

[39] S. Mondol, S. Kashyap, S. Kumar, K. Chattopadhyay, Improvement of high temperature strength of 2219 alloy by Sc and Zr addition through a novel three-stage heat treatment route, Mater. Sci. Eng.: A 732 (2018) 157–166, https://doi.org/10.1016/j.msea.2018.07.003.

[40] A. Da Silva, F. Belelli, G. Lupi, F. Bruzzo, B. Brandau, L. Maier, A. Pesl, J. Frostevarg, R. Casati, E. Lopez, A.F.H. Kaplan, Influence of aluminium powder aging on Directed Energy deposition, Mater. Des. 218 (2022), 110677, https://doi.org/10.1016/j.matdes.2022.110677.

[41] T. Fedina, F. Belelli, G. Lupi, B. Brandau, R. Casati, R. Berneth, F. Brueckner, A.F. H. Kaplan, Influence of AlSi10Mg powder aging on the material degradation and its processing in laser powder bed fusion, Powder Technol. 412 (2022), 118024, https://doi.org/10.1016/j.powtec.2022.118024.

[42] G.C. Smith, Age hardening of metals, Prog. Met. Phys. 1 (1949) 163–234, https://doi.org/10.1016/0502-8205(49)90006-4.

[43] N.Yu Zolotorevsky, A.N. Solonin, A.Yu Churyumov, V.S. Zolotorevsky, Study of work hardening of quenched and naturally aged Al–Mg and Al–Cu alloys, Mater. Sci. Eng.: A 502 (2009) 111–117, https://doi.org/10.1016/j.msea.2008.10.010.

[44] R. Casati, J.N. Lemke, A.Z. Alarcon, M. Vedani, Aging Behavior of High-Strength Al Alloy 2618 Produced by Selective Laser Melting, Metall. Mater. Trans. A 48 (2017) 575–579, https://doi.org/10.1007/s11661-016-3883-y.

[45] S. Kumar Makineni, S. Sugathan, S. Meher, R. Banerjee, S. Bhattacharya, S. Kumar, K. Chattopadhyay, Enhancing elevated temperature strength of copper containing aluminium alloys by forming L12 Al3Zr precipitates and nucleating θ'' precipitates on them, Sci. Rep. 7 (2017) 11154, https://doi.org/10.1038/s41598-017-11540-2.

[46] Z. Jia, J.-P. Couzinié, N. Cherdoudi, I. Guillot, L. Arnberg, P. Åsholt, S. Brusethaug, B. Barlas, D. Massinon, Precipitation behaviour of Al3Zr precipitate in Al–Cu–Zr and Al–Cu–Zr–Ti–V alloys, Trans. Nonferrous Met. Soc. China 22 (2012) 1860–1865, https://doi.org/10.1016/S1003-6326(11)61398-8.

[47] J.D. Robson, P.B. Prangnell, Modelling Al3Zr dispersoid precipitation in multicomponent aluminium alloys, Mater. Sci. Eng.: A 352 (2003) 240–250, https://doi.org/10.1016/S0921-5093(02)00894-8.

[48] Y. Wang, X. Lin, N. Kang, Z. Wang, Y. Liu, W. Huang, Influence of post-heat treatment on the microstructure and mechanical properties of Al-Cu-Mg-Zr alloy manufactured by selective laser melting, J. Mater. Sci. Technol. 111 (2022) 35–48, https://doi.org/10.1016/j.jmst.2021.09.036.

[49] P.N.T. Unwin, G.W. Lorimer, R.B. Nicholson, The origin of the grain boundary precipitate free zone, Acta Metall. 17 (1969) 1363–1377, https://doi.org/10.1016/0001-6160(69)90154-0.

[50] T. Liu, X. Su, Y. Liu, C. Wu, J. Wang, Microstructural Evolution of Aluminum Alloy 2618 During Homogenization and Its Kinetic Analysis, High. Temp. Mater. Process. 33 (2014) 85–94, https://doi.org/10.1515/htmp-2013-0029.

[51] S. Toschi, E. Balducci, L. Ceschini, E.A. Mørtsell, A. Morri, M. Di Sabatino, Effect of Zr Addition on Overaging and Tensile Behavior of 2618 Aluminum Alloy, Metals 9 (2019) 130, https://doi.org/10.3390/met9020130.

[52] L. Kovarik, S.A. Court, H.L. Fraser, M.J. Mills, GPB zones and composite GPB/GPBII zones in Al–Cu–Mg alloys, Acta Mater. 56 (2008) 4804–4815, https://doi.org/10.1016/j.actamat.2008.05.042.

[53] K. Yu, W. Li, S. Li, J. Zhao, Mechanical properties and microstructure of aluminum alloy 2618 with Al3(Sc, Zr) phases, Mater. Sci. Eng.: A 368 (2004) 88–93, https://doi.org/10.1016/j.msea.2003.09.092.

[54] A. De Luca, D.N. Seidman, D.C. Dunand, Effects of Mo and Mn microadditions on strengthening and over-aging resistance of nanoprecipitation-strengthened Al-Zr-Sc-Er-Si alloys, Acta Mater. 165 (2019) 1–14, https://doi.org/10.1016/j.actamat.2018.11.031.

[55] W.H. Kan, Y. Nadot, M. Foley, L. Ridosz, G. Proust, J.M. Cairney, Factors that affect the properties of additively-manufactured AlSi10Mg: Porosity versus microstructure, Addit. Manuf. 29 (2019), 100805, https://doi.org/10.1016/j.addma.2019.100805.

[56] F.H. Kim, S.P. Moylan, T.Q. Phan, E.J. Garboczi, Investigation of the Effect of Artificial Internal Defects on the Tensile Behavior of Laser Powder Bed Fusion 17–4 Stainless Steel Samples: Simultaneous Tensile Testing and X-Ray Computed Tomography, Exp. Mech. 60 (2020) 987–1004, https://doi.org/10.1007/s11340-020-00604-6.

[57] U. Tradowsky, J. White, R.M. Ward, N. Read, W. Reimers, M.M. Attallah, Selective laser melting of AlSi10Mg: Influence of post-processing on the microstructural and tensile properties development, Mater. Des. 105 (2016) 212–222, https://doi.org/10.1016/j.matdes.2016.05.066.

[58] P. Shen, E.M. Elgallad, X.-G. Chen, On the Aging Behavior of AA2618 DC Cast Alloy, in: B.A. Sadler (Ed.), Light Metals 2013, Springer International Publishing, Cham, 2016, pp. 373–377, https://doi.org/10.1007/978-3-319-65136-1_65.

[59] R. Ivanov, A. Deschamps, F. De Geuser, Clustering kinetics during natural ageing of Al-Cu based alloys with (Mg, Li) additions, in: Acta Materialia, 157, 2018, pp. 186–195, https://doi.org/10.1016/j.actamat.2018.07.035.

[60] A. Mehta, L. Zhou, T. Huynh, S. Park, H. Hyer, S. Song, Y. Bai, D.D. Imholte, N. E. Woolstenhulme, D.M. Wachs, Y. Sohn, Additive manufacturing and mechanical properties of the dense and crack free Zr-modified aluminum alloy 6061 fabricated by the laser-powder bed fusion, Addit. Manuf. 41 (2021), 101966, https://doi.org/10.1016/j.addma.2021.101966.

[61] A.M. Agogino, Notch effects, stress state, and ductility, J. Eng. Mater. Technol. 100 (1978) 348–355, https://doi.org/10.1115/1.3443503.

[62] G. Gottstein, Physical Foundations of Materials Science, Springer-Verlag,, Berlin Heidelberg, 2004, https://doi.org/10.1007/978-3-662-09291-0.

[63] J.G. Kaufman, Understanding the Aluminum Temper Designation System, 2013. ⟨https://materialsdata.nist.gov/handle/11115/186⟩ (accessed June 10, 2021).

[64] J.W. Bray, ASM handbook. 2: Properties and selection: nonferrous alloys and special-purpose materials, 7. print, ASM International, Materials Park, Ohio, 2007.

[65] H. Zhang, H. Zhu, T. Qi, Z. Hu, X. Zeng, Selective laser melting of high strength Al–Cu–Mg alloys: Processing, microstructure and mechanical properties, Mater. Sci. Eng.: A 656 (2016) 47–54, https://doi.org/10.1016/j.msea.2015.12.101.